

Characterization of surface motion patterns in highly deformable soft tissue organs from dynamic Magnetic Resonance Imaging

Karim Makki ^{a,*}, Amine Bohi^{a,*}, Augustin C. Ogier^a, and Marc Emmanuel Bellemare^a

^a*Aix Marseille Univ, Université de Toulon, CNRS, LIS, Marseille, France*

^{*} *These authors contributed equally to this work*

Abstract

In this work, we present a pipeline for characterization of bladder surface dynamics during deep respiratory movements from dynamic Magnetic Resonance Imaging (MRI). Dynamic MRI may capture temporal anatomical changes in soft tissue organs with high-contrast but the obtained sequences usually suffer from limited volume coverage which makes the high resolution reconstruction of organ shape trajectories a major challenge in temporal studies. For a compact shape representation, the reconstructed temporal data with full volume coverage are first used to establish a subject-specific dynamical 4D mesh sequences using the large deformation diffeomorphic metric mapping (LDDMM) framework. Then, we performed a statistical characterization of organ shape changes from mechanical parameters such as mesh elongations and distortions. Since shape space is curved, we have also used the intrinsic curvature changes as metric to quantify surface evolution. However, the numerical computation of curvature is strongly dependant on the surface parameterization (*i.e.* the mesh resolution). To cope with this dependency, we propose a non-parametric level set method to evaluate spatio-temporal surface evolution. Independent of parameterization and minimizing the length of the geodesic curves, it shrinks smoothly the surface curves towards a sphere by minimizing a Dirichlet energy. An Eulerian PDE approach is used for evaluation of surface dynamics from the curve-shortening flow. Results demonstrate the numerical stability of the derived descriptor throughout smooth continuous-time organ trajectories. Intercorrelations between individuals' motion patterns from different geometric features are computed using the Laplace–Beltrami Operator (LBO) eigenfunctions for spherical mapping.

Keywords: Shape analysis, Motion estimation, Dynamic MRI, Geodesic distances, Differential geometry, Geometric features

1. Introduction

Pelvic floor disorders affect approximately 50% of women older than 50 years [1]. Related health problems such as urinary and fecal incontinences get worse with age which affects activities of daily living. To help surgeons and clinicians for better understanding these disorders, it is crucial to characterize the normative pelvic floor dynamics in healthy women before focusing pathomechanics studies.

In vivo characterization of the dynamical behaviour of human joints, organs, and soft tissues during daily physical activities remains challenging because of the complexity and the non-linearity of their shape dynamics [2, 3, 4, 5, 6, 7].

Statistical shape analysis tools have been used effectively in medical imaging to help understand patterns in large clinical data sets and to characterize the functioning soft tissue of organs or shapes undergoing large and non-linear deformations in terms of geometry and time dynamics [8], [9], [10], [11], [12], [13]. For instance, simply encoding deformations with a vector space of displacement fields is not sufficient to identify morphological changes in highly deformable shapes regarding the complexity of their topology (i.e. the Jacobian of the deformation field is not a meaningful parameter in statistical characterization). In this context, space-time statistics should be based on robust and stable geometric shape descriptors and surface features. The temporal feature changes may characterize the local shape deformations while preserving their topologies. Since shape space is a curved surface, statistical tools derived from Euclidean geometry are not well adapted in this context which have motivated researchers to employ Riemannian geometry for generating shape trajectories belonging to non-linear manifolds [14, 15]. Relying on the notion of geodesic distances on manifolds to compute the shortest paths between two points on a curved surface [16], these tools cover topics that start from the fundamentals of general relativity theory [17].

In practice, several studies for characterizing spatio-temporal shape trajectories have used longitudinal datasets and the goal was to quantify the shape growth over a long period of time [18] (intrasubject variations in geometry) or the shape variability in an inter-subject context (*e.g.* for atlas building at the population level [19]). Longitudinal data consists of a collection of stationary scans (*e.g.* conventional high-resolution MRI scans) portraying anatomical changes during a large period of time (over weeks or months, depending on the studied pathology or phenomena). Such studies have served to highlight the need for clinicians to understand anatomical changes occurring during development or disease progression (*e.g.* linear geodesic regression model for shape time-series with sparse parameters [12, 10]).

As compared to longitudinal studies, temporal studies using dynamic MRI may non-invasively capture anatomical changes during motion over a short period of time but they add a set of new challenges : (1) less spatio-temporal resolution of anatomical data sequences, (2) higher sensitivity to motion artifacts, (3) and an increased effect of image noise. Surmounting these difficulties arising in the data sequences represents a newest challenge especially when a high-resolution temporal reconstruction of shape trajectory becomes necessary for performing statistically significant studies.

In this paper, we have employed diffeomorphic statistical shape tools to evaluate shape deformations during daily living motions : starting from sets of high resolution reconstructed bladder temporal volumes, we have first employed the LDDMM to encode the organ's large deformations with a reduced number of significant surface points while covering properties in shape topology. A structured dynamical meshes for the organ surface are then established to derive biomechanical parameters.

Then, characterizations of organ shape dynamics are performed with use of : surface intrinsic properties derived from local curvature changes to capture tangential surface de-

formations ; surface mesh distortion highlighting sharp geometric variations ; and also mesh elongations to capture the longitudinal and transverse shape variations. A new geometric feature is also proposed, to detect non-salient motion patterns from geodesic shortest length paths for mapping a shape to a sphere. It satisfies the "invariance" conditions of Kendall's shape space [20], by filtering out location, size and rotation. This feature may capture surface variation, with no need to compute Riemann's tensor. Computing tensors not only incurs high computational costs but also impacts numerical stability [21]. Results demonstrate that the proposed feature is numerically stable and robust face to motion repeatability for long reconstructed shape trajectories.

Since we are interested in comparing shapes in terms of their geometry rather than their size, we performed shape comparisons in a common *shape space*. Motion patterns derived from the different feature vectors were projected to the unit sphere \mathcal{S}^2 (point-to-point anatomical correspondences between these geometric features are established across subjects), in order to compute intercorrelations between individuals' motion patterns with the help of the Laplace–Beltrami Operator (LBO) eigenfunctions for spherical mapping [22, 23].

2. Related work

In the literature, some studies have attempted to non invasively quantify or model human soft tissues, organs, and skeleton in vivo dynamics during daily living activities [24, 9, 7]. In the context of pelvic floor dynamics, most studies were purely presented from a biomechanical point of view, and aimed essentially at modelling pelvic organ deformations with finite element simulations due to limitations of spatial resolution of dynamic MRI data [25, 26]. In [27, 7] a first attempt to quantify the ankle joint motion patterns through a combination of static and dynamic MRI data is presented. A tracking of bones and surrounding soft tissues is performed by estimating a dense deformation field covering the entire field of view from the static scan to dynamic time frames using the Log Euclidean Polyrigid registration framework (LEPF) [28]. A similar study for spatio-temporal reconstruction of abdominal organ non-linear dynamics during forced breathing exercises using diffeomorphic registration is introduced in [29]. Promising results were obtained, showing the bladder in its 3D complexity during deformation due to strain conditions with an estimation of the most deformed tissue areas. These high-resolution temporal data are then employed to introduce a compact characterization of bladder surfaces in [30].

In [26], 2D dynamic MRI images are combined with 3D biomechanical models in order to extrapolate the complete 3D dynamic motion of abdominal organs. This methodology was validated by checking the fact that the reconstructions were well conducted from the first scan towards the end of dynamic sequence. However, the validation itself was not founded on a clinically relevant ground truth (i.e. the validation was not performed in the high resolution domain). Furthermore, only two simulated sequences have been used to validate the model. To achieve full volume coverage, these issues have already been addressed in [29], where the reconstruction of realistic 3D bladder trajectories was assessed by preserving the static volume undergoing large deformations to fit each of the low resolution volumes. The reconstruction pipeline was based on diffeomorphic registration (ANTs tools) to perform

inter-slice registration over a restricted field of view (using bounding boxes around the organ of interest to accelerate the alignment convergence). A set of different configurations for dynamic data acquisitions were used and the reconstruction consisted of filling the inter-slice gaps.

3. Methods

3.1. Dynamic quadrilateral mesh

3.1.1. Quadrilateral mesh generation

To encode the shape surface with an extremely low number of meaningful variables, we have first extracted iso-surfaces from the reconstructed organ volumes (*i.e.* 3D binary masks) at the first time frame using the marching cubes algorithm. The marching squares/cubes is the standard algorithm to extract iso-curves/surfaces from a discretized image/volume [31]. Then, and to take into account the complexity of the organ shape, a topologically regular quadrilateral mesh of the organ surface is generated from the first reconstructed volume, using a robust algorithm presented in [32]. This algorithm is robust enough to establish a convex quad mesh for the organ surface since it avoids irregularity problems at the poles, as encountered in [25], despite some singularities which can be regularized by mesh upsampling in order to obtain a pure quad mesh for which the vertices are first geodesically equidistant. Fig. 1 illustrates the quality of the obtained mesh. In a second step, we propose to track the mesh vertices during respiratory motion while preserving their connections (*i.e.* while keeping the faces unchanged). This allows for constructing a spatio-temporal structured meshes which might also be used for deriving some biomechanical properties of the organ dynamics such as strains and stresses using finite element methods which are required for establishing a biomechanical model for the organ dynamics (*i.e.* pure quad meshes are often desired in CAD applications).

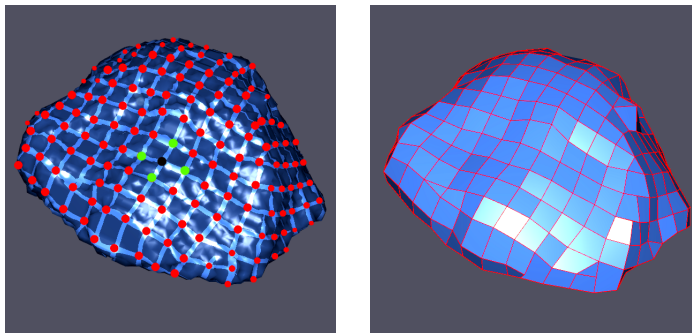


FIGURE 1 – Quadrilateral mesh for the organ surface, from left to right : the position field, and the output mesh.

3.1.2. Estimation of smooth vertex trajectories

To determine point correspondences, a mesh-to-volume registration is performed : we propose to track the set of mesh vertices during the bladder deformations using the LDDMM

framework [33] that has been heuristically shown to produce natural deformation paths in the space of diffeomorphisms. This framework which is based on Hamiltonian dynamics and statistical mechanics allows one to provide an hypothesis compatible with the physics of deformations by estimating geodesic shape curves without having to use point-to-point correspondences between source and target point sets. A smooth and continuous-time trajectory of each vertex is estimated throughout the organ range of motion (vertices travel along geodesic curves).

The principle of control-points-based LDDMM for estimating a diffeomorphic mapping is as follows :

Given a set of N control points $\{q_i\}_{i \in 1, \dots, N}$, and a set of N corresponding momentum vectors of \mathbb{R}^3 $\{\mu_i\}_{i \in 1, \dots, N}$, the velocity vector in the tangent space $\mathcal{T}_x \mathcal{M}$ of the parametric surface \mathcal{M} at a point $x \in \mathcal{M}$, is obtained through the use of a Gaussian convolution filter :

$$v : x \in \mathcal{M} \mapsto v(x) = \sum_{i=1}^N K(x, q_i) \cdot \mu_i \quad (1)$$

where $K(x_i, x_j) = \exp(-\|x_i - x_j\|^2 / \sigma^2)$ is a Gaussian kernel.

The temporal evolution of the organ velocity vector field can be modeled by the following Hamilton's equations of motion :

$$\begin{cases} \dot{q}(t) = K(q(t), q(t)) \cdot \mu(t) \\ \dot{\mu}(t) = -\frac{1}{2} \nabla_q \{K(q(t), q(t)), \mu(t)^\top \mu(t)\} \end{cases} \quad (2)$$

The solutions to this Hamiltonian are then the same as the geodesics on a Riemannian manifold. The numerical integration of these PDEs, performed using a second-order Runge-Kutta scheme, gives the flow of a time-dependent velocity vector field parameterized with $q(t)$ and $\mu(t)$:

$$v : x \in \mathbb{R}^3 \times t \in [0, 1] \mapsto v(x, t) = \sum_{i=1}^N K(x, q_i(t)) \cdot \mu_i(t) \quad (3)$$

The temporal displacement of each tracked point $x \in \mathcal{M}$ is governed by the following autonomous first order ODE :

$$\dot{x}(t) = v(x(t), t) \quad s.t \quad x(0) = x \quad (4)$$

Finally, the solution of this ODE yields a flow of diffeomorphisms starting from the source points (i.e. starting from the identity in the space of transformations), $\Phi_{q, \mu}(\cdot, t) : \mathbb{R}^3 \times [0, 1] \mapsto \mathbb{R}^3$, such that $\Phi_{q, \mu}(\cdot, 1) = Id + \int_0^1 v(\Phi_{q, \mu}(\cdot, t)) dt$ is the end-point of the geodesic flow matching the given point sets.

The overall algorithm for vertex tracking is described in Algorithm 1, with the following notations : L is the length of the dynamic sequence ; \mathcal{M}_t gives the locations of mesh vertices at time t ; \mathcal{C}_t is the entire 3D surface point cloud at time t (\mathcal{M}_t is a proper subset of \mathcal{C}_t). Note that the registration problem is solved by iteratively minimizing the following loss function :

$$f(q, \mu) = d(\mathcal{C}_{t+1}, \Phi_{q, \mu}(\mathcal{M}_t)) + R(q, \mu) \quad (5)$$

where the first term measures data-attachment while the second regularization term represents the norm of the deformation. Some results of our tracking algorithm are illustrated in Fig. 2.

Algorithm 1 LDDMM-based 4D quad mesh generation

- **Input** : Initial mesh structure (F, \mathcal{M}_0) .
 - **Motion estimation** : Estimate forward successive vertex trajectories using the LDDMM $\{\mathcal{M}_{t+1}\}_{t=0,\dots,L-1}$ such that $\mathcal{M}_t \subset \mathcal{C}_t$, for $t = 0, \dots, L - 1$, by aligning \mathcal{M}_t and \mathcal{C}_{t+1} .
 - **Output** : 4D quad mesh sequence (F, \mathcal{M}_t) .
-

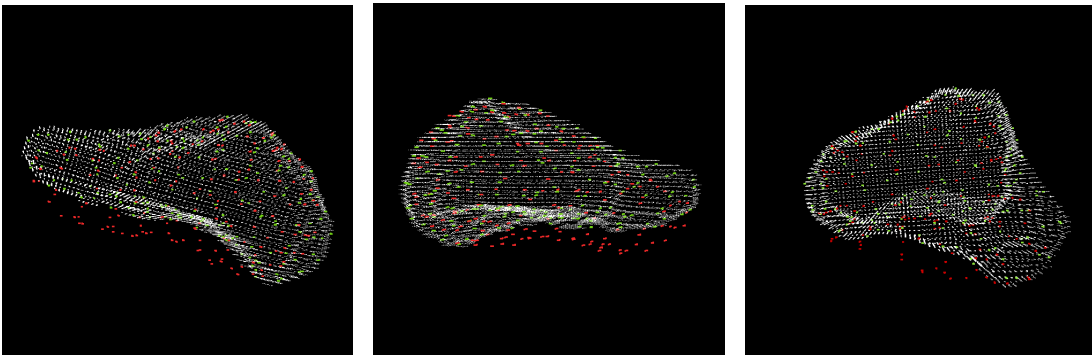


FIGURE 2 – Pointset tracking : \mathcal{M}_0 in red, \mathcal{M}_t in green, and \mathcal{C}_t in white.

3.2. Shape descriptors

In this section, we present the geometric descriptors that we have used to characterize the organ dynamics from the reconstructed quad meshes.

3.2.1. Mesh elongation and distortion

Shape elongations and distortions have been used in medical imaging, in particular to characterize the deformations of the pelvic organs in the plane from dynamical organ contour points [34]. However, 2D+t shape processing can result in biased estimation of common measures because of the out-of-plane problem. To overcome these limitations, an extension of these measures to 3D space was performed by adopting a simple generalization of them :

Mesh elongation :

The mesh elongation also called the Green-Lagrange deformation descriptor is a commonly used feature in biomechanics for characterizing local mesh deformations based on the spacing changes in the neighborhood of each vertex. Let's have a vertex $V_i^j(t)$ and its four nearest neighbors $\{V_{i+1}^j(t), V_{i-1}^j(t), V_i^{j+1}(t), V_i^{j-1}(t)\}$ belonging to the mesh at the $(t)^{th}$ time frame, and a vertex $V_i^j(t+1)$ and its neighbors $\{V_{i+1}^j(t+1), V_{i-1}^j(t+1), V_i^{j+1}(t+1), V_i^{j-1}(t+1)\}$,

their homologous vertices at the $(t + 1)^{th}$ timeframe. We compute $\hat{d}(t)$ and $\hat{d}(t + 1)$ the average Euclidean distances between $V_i^j(t)$ and its neighbors (resp. between $V_i^j(t + 1)$ and its neighbors). Then, the elongation measure is given by :

$$E(t) = \frac{\hat{d}(t) - \hat{d}(t + 1)}{2 \times \hat{d}(t + 1)} \quad (6)$$

If $E(t) = 0$, then no deformation has occurred, else if $E(t) > 0$, the neighborhood of the vertex has expanded. Otherwise, the neighborhood has shrunk.

Mesh distortion :

The dihedral angles are defined as the angles between the two normal vectors to each two adjacent faces [35]. And the temporal change of these angles during motion is considered as the temporal distortion of the quad mesh.

For two adjacent quadrilateral faces $F_1 = \{V_1, V_2, V_3, V_4\}$ and $F_2 = \{V_1, V_2, V'_3, V'_4\}$, with normals N_1 and N_2 , respectively, the local dihedral angle is computed as follows :

$$\theta = \arccos \left(\frac{N_1 \cdot N_2}{\|N_1\| \times \|N_2\|} \right) \quad (7)$$

Let $V_i^j(t)$ and $V_i^j(t + 1)$ be the mesh vertices corresponding to the same tracked surface point at times t and $t + 1$, respectively. Assuming that the adjacent faces to each vertex of the initial quad mesh (at $t = 0$) were maintained the same throughout the sequence, then both vertices have always the same adjacent faces that we note $\{F_1(t), F_2(t), F_3(t), F_4(t)\}$. If we consider $\theta(t)$ and $\theta(t + 1)$ as the maximal dihedral angles between each pair of faces adjacent to vertices $V_i^j(t)$ and $V_i^j(t + 1)$, respectively. Then, the temporal mesh distortion around V_i^j is determined by :

$$D(t) = | \theta(t + 1) - \theta(t) | \quad (8)$$

If $D(t) = 0$, then no local deformation has occurred. Otherwise, the neighborhood has distorted.

3.2.2. A novel geodesic-based feature for characterization of 3D shapes :

In this section, we propose a robust global feature to detect the surface variation in terms of concavity and convexity with smooth transitions in-between from a level set function obtained by minimizing the Dirichlet energy inside the surface between shape and a surrounding sphere. This gives a set of paths of minimum Dirichlet energy (*i.e.* a geodesic flow) that are used to capture the tangential evolution of shape surface.

Definition Given an open set $\Omega \subseteq \mathbb{R}^n$ and a differentiable function $h : \Omega \rightarrow \mathbb{R}$, the Dirichlet energy of h is defined by the following positive real number :

$$E[h] = \frac{1}{2} \int_{x \in \Omega} \|\nabla h(x)\|^2 dx \quad (9)$$

where $\nabla h : \Omega \rightarrow \mathbb{R}^n$ denotes the gradient vector field of h .

Solving Laplace's equation $\Delta h(x) = 0, \forall x \in \Omega$, subject to appropriate Dirichlet boundary conditions, is equivalent to solving the variational problem of finding a function h that satisfies the boundary conditions and has minimal Dirichlet energy. h is also called a level set function.

For a closed 3D shape S , the *proposed* feature can be numerically approximated using an Eulerian PDE approach, involving the following steps.

Definition of Dirichlet boundary conditions :

To initialize the algorithm, the binary mask of the shape is eroded with a cross-shaped structuring element which is best suited for fine structures. The choice of the structuring element is of great importance for preserving, as much as possible, the topology of any arbitrary shape. This gives the eroded binary mask that we note S_e . Then, we use a PCA analysis of S in order to determine the radius R of the surrounding sphere S_s for which the center coincides with the shape centroid. The radius R is proportional to the length l of the principal axis of inertia ($R = 0.8l$). At this level, all the shape contour points will be located between two non-intersecting boundaries : $S_{in} = S_e$, and $S_{out} = \bar{S}_s$.

The next steps consist of computing the length of the shortest geodesic paths from S_{in} to S_{out} in a bijective fashion.

Solving the Laplace equation, subject to Dirichlet boundary conditions :

This primordial step consists of solving the Dirichlet problem, also known as the problem of finding a function which solves a specified PDE inside a region that takes prescribed values on its boundaries. The Dirichlet energy is intimately connected to Laplace's equation. In practice, we are looking for an elliptic twice-differentiable function $h : \mathbb{R}^3 \rightarrow \mathbb{R}$ which satisfies the Laplace's PDE $\Delta h = \text{div}(\text{grad}(h)) = 0$ inside the region $\Omega = \overline{S_{in} \cup S_{out}}$, subject to the Dirichlet boundary conditions $h(\partial S_{in}) = 10^4$ and $h(\partial S_{out}) = 0$ (*i.e.* h is the function that has minimal Dirichlet energy for all $x \in \Omega$, also called the harmonic interpolant in potential theory). The physical intuition behind is to determine the equilibrium heat distribution in a perfectly symmetric spherical room since the divergence of the gradient vector field corresponds to some kind of fluid flow.

To approximate the numerical solution of Laplace's equation, we use the Jacobi iterative relaxation method which is simple to implement and which allows fast approximation of the solution in cartesian coordinates :

$$\begin{aligned}
 h_{t+1}(i, j, k) = & \frac{1}{2(d_x^2 d_y^2 + d_x^2 d_z^2 + d_y^2 d_z^2)} (d_y^2 d_z^2 [h_t(i + d_i, j, k) + h_t(i - d_i, j, k)] + d_x^2 d_z^2 [h_t(i, j + d_j, k) \\
 & + h_t(i, j - d_j, k)] + d_x^2 d_y^2 [h_t(i, j, k + d_k) + h_t(i, j, k - d_k)])
 \end{aligned}
 \tag{10}$$

where t is the iteration index. In this work, we process reconstructed data with an isotropic voxel spacing of $1 \times 1 \times 1 \text{mm}$ (*i.e.* $d_x = d_y = d_z = 1$).

Computing the normal vectors to the tangent planes to the harmonic layers :

We determine elementary normal paths from S_{in} to S_{out} , *i.e.* from the normalized gradient vector field of the harmonic interpolant h , $\vec{T} = \frac{\nabla h}{\|\nabla h\|} = (T_x, T_y, T_z)^T$. This normal velocity vector field allows for a bijective mapping between pairs of points (*i.e.* a one-to-one mapping).

An Eulerian PDE computational scheme :

We estimate the lengths of optimal geodesic paths between the two boundaries, by solving a couple of Eulerian PDEs : $\nabla L_0 \cdot \vec{T} = -\nabla L_1 \cdot \vec{T} = 1$. L_0 and L_1 are first initialized to 0.5 and then iteratively updated using a symmetric relaxation Gauss-Seidel method :

$$\frac{L_0^{t+1}[i,j,k]}{\alpha} = 1 + |T_x| L_0^t[i \mp 1, j, k] + |T_y| L_0^t[i, j \mp 1, k] + |T_z| L_0^t[i, j, k \mp 1] \quad (11)$$

$$\frac{L_1^{t+1}[i,j,k]}{\alpha} = 1 + |T_x| L_1^t[i \pm 1, j, k] + |T_y| L_1^t[i, j \pm 1, k] + |T_z| L_1^t[i, j, k \pm 1] \quad (12)$$

$$\text{where : } \begin{cases} m \pm 1 = m + \text{sgn}(T); & m \mp 1 = m - \text{sgn}(T) \\ \text{for } m \in \{i, j, k\}; & \text{and } \alpha = \frac{1}{|T_x| + |T_y| + |T_z|} \end{cases}$$

with : $\text{sgn}(\cdot)$ is the sign function, $L_0(x)$ is the length of the optimal geodesic path from the point $x = (i, j, k)$ to S_{in} , while $L_1(x)$ is the length of the optimal geodesic path from x to S_{out} . The sum of these two lengths $G(x) = L_0(x) + L_1(x)$, defined as *thickness* in [36], represents in fact the length of the optimal geodesic path from S_{in} to S_{out} that passes through x . These geometric methods which are based on a fully Eulerian point of view allow one to handle time derivatives with finite differences in a bounded physical domain that exhibit large deformations and topology changes.

Convergence criterion :

The numerical solution of Laplace's equation is iteratively relaxed by finite differences. All grid points inside Ω are visited at each iteration. A convergence criterion can be defined by the following expression based on the total field energy over Ω :

$\epsilon_t = \sum_{x \in \Omega} \sqrt{(\frac{\Delta h_t}{di})^2 + (\frac{\Delta h_t}{dj})^2 + (\frac{\Delta h_t}{dk})^2}$, where $\frac{\Delta h_t}{di} = \frac{h_t(i+di,j,k) - h_t(i-di,j,k)}{2}$. The Jacobi iterative computational scheme of eq (10) converges when the ratio $\epsilon = \frac{\epsilon_t - \epsilon_{t+1}}{\epsilon_t}$ becomes smaller than a user-defined threshold (typically about 10^{-5}). To speed up the algorithm, we strongly recommend to keep the number of iterations as a user defined parameter in order to avoid the repeated evaluation of ϵ at each iteration. A total number of 200 iterations is used for solving the Laplace's equation and the pair of PDEs in this work.

Proposed feature to characterizing the surface variation :

Finally, we define a flexible feature by the following application $\tilde{f} : \mathbb{R}^3 \rightarrow \mathbb{R}$:

$$\tilde{f}(x) = \frac{R}{G(x)} \quad (13)$$

Note that $L_1 \gg L_0$ for all the contour points so that $G \simeq L_1$ and only one PDE has to be solved to calculate the feature function. The function \tilde{f} has the potential to characterize surface variation and to smoothly delineate between concave, convex and flat regions as illustrated in Fig 6 for both torus and ellipsoid. Relatively, the largest feature values correspond to the most convex areas in the surface while the smallest values correspond to the most concave areas. The proposed feature values exhibit smooth transitions between concave and convex regions of the surface. Furthermore, this feature is invariant to scaling since the sphere radius is proportional to the length of the principal axis of inertia of the shape; invariant to rotation thanks to spherical symmetry; and also invariant to translation since the sphere center coincides with the shape centroid. An illustration of all the previous steps is presented in Fig. 3.

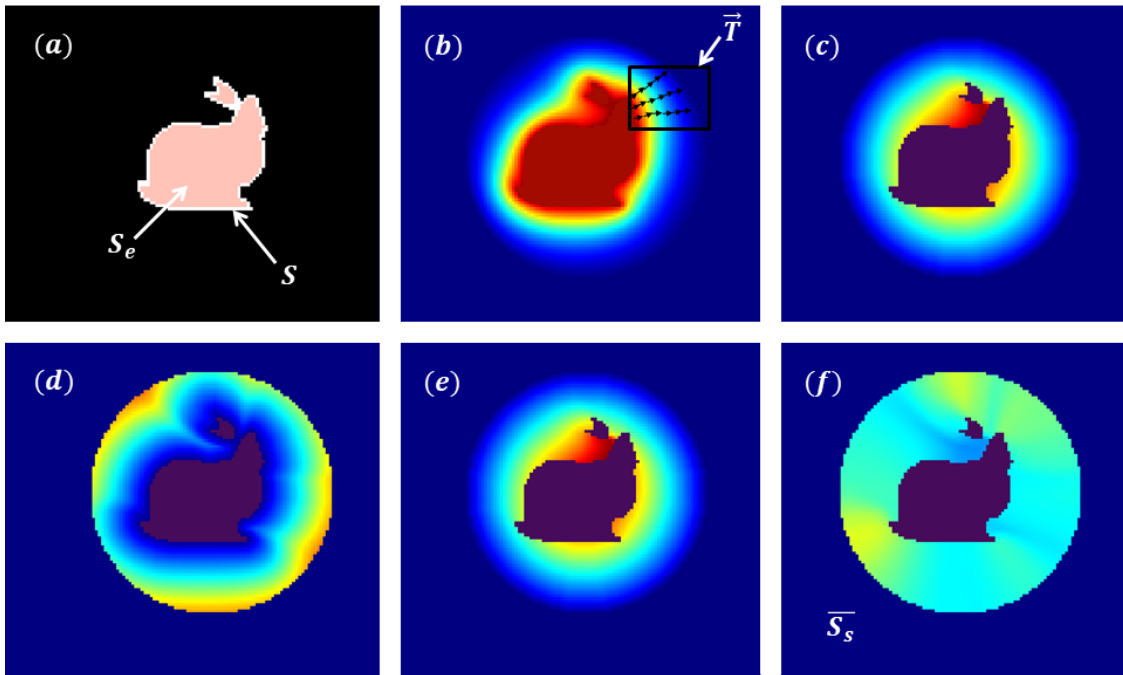


FIGURE 3 – Proposed method (Stanford Bunny example) : (a) binary mask and its eroded; (b) solution of the Laplace equation h ; (c) length of the geodesic path from x to the surrounding sphere L_1 ; (d) length of the geodesic path from x to the inner boundary L_0 ; (e) length of the resulting geodesic path G ; and (f) feature values \tilde{f} between the two boundaries.

4. Experiments and Results

4.1. Data set

4.1.1. Realistic dynamic MRI data

Pelvis areas of seven healthy participants were imaged with a 1.5T MRI scanner (MAGNETOM Avanto, Siemens AG, Healthcare Sector, Erlangen, Germany) using a spine/phased array coil combination. The scanning protocol included one high resolution static 3D scan of the stationary pelvic floor, T_1/T_2W bSSFP images (TR : $170.84ms$, echo time : $0.99ms$, flip angle : 32° , field of view : $277 \times 320mm^2$, pixel size : $0.83 \times 0.83mm^2$, slice thickness : $2mm$). For dynamic MRI acquisitions, T_1/T_2W bSSFP images (TR : $125ms$, echo time : $1.25ms$, flip angle : 52° , field of view : $299 \times 350mm^2$, pixel size : $1.36 \times 1.36mm^2$, slice thickness : $6mm$, multi-planar configuration) were recorded during a 1 :20-minutes forced breathing exercise. During this exercise, the subject alternately inspired and expired at maximum capacity. Subjects were also instructed to increase the pelvic pressure to the maximum inspiration and contrary to contract the pelvic floor during the expiration. These actions increased the intra-abdominal pressure, causing deformities of the pelvic organs. The study was approved by the local human research committee and was conducted in conformity with the Declaration of Helsinki. Since no extraneous liquids were injected into pelvic cavities in this study, only the segmentation of the bladder was performed and the analysis focused exclusively on this organ. For each subject, the three-dimensional dynamic sequences acquired in multi-planar configurations allowed the reconstruction of nearly 400 bladder volumes generated at a rate of 8 volumes per second.

4.1.2. Data simulation

To evaluate the capability of each geometric descriptor in detecting abnormalities in bladder dynamics during breathing exercises, we have simulated a 3D+t high resolution MRI sequence by estimating a continuous-time trajectory of the organ volume using a Log Euclidean Polyaffine registration framework [28] to excite the organ deformation from the interior with locally controlled properties. The organ volume in the static scan is divided into four non-intersecting regions and an affine transformation is associated to each region or component (we have only used component-wise scaling transforms in such a way that the organ volume is still preserved throughout the sequence). A first motion cycle is simulated by estimating a flow of invertible diffeomorphisms for mapping the organ volume from resting state (i.e. organ volume in the stationary scan) towards the maximum of inspiration state (largest deformation). Then, the inverse trajectory for coming back to the resting state is obtained by smoothly interpolating the inverse of the simulated polyaffine transformations. Finally, this motion cycle is repeated 8 times for repeatability measures.

In practice, We simulated a large deformation to make the organ fall down by maximum of inspiration which allow the floor of the bladder to sag through the muscle and ligament layers. This abnormal kind of motion occurs frequently in women with uterine and bladder Prolapse for which the bladder can create a bulge into the vagina because of the weakness of their pelvic muscles and ligaments. Figure 4 illustrates the simulated organ trajectory from resting state to the maximum of inspiration. This simulated sequence, for which the shape

trajectory is well known, will serve to compare the different features used in this study in terms of stability and measure repeatability during forward organ movement.

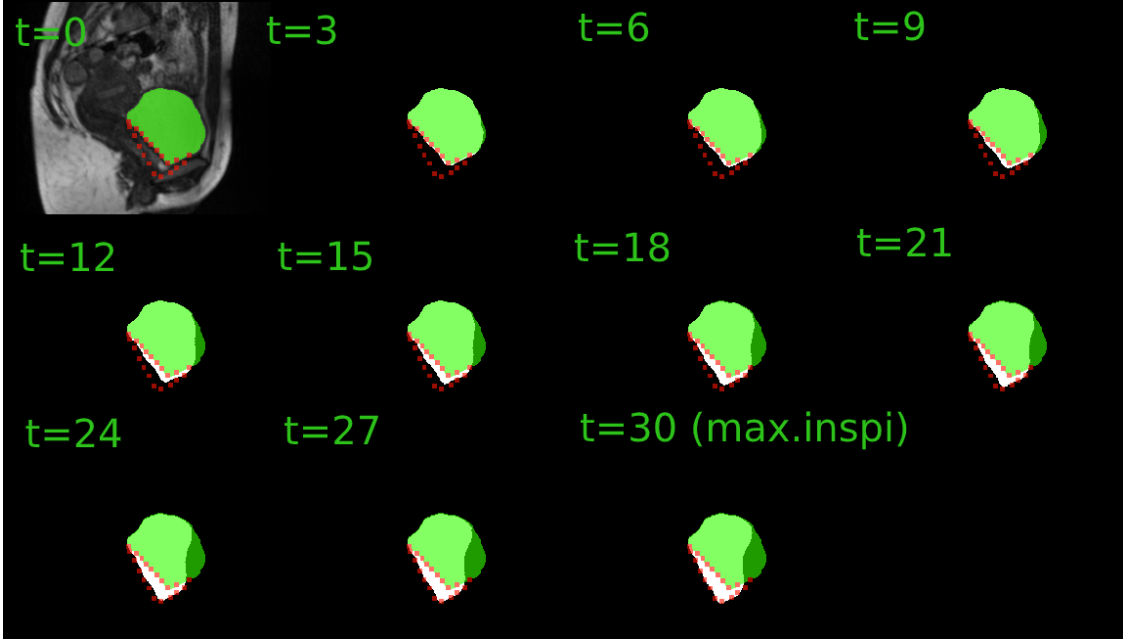


FIGURE 4 – Simulation of large deformations using the LEPF, the green mask corresponds to the bladder segmentation at the resting state, the white segmentations correspond to the temporal organ positions ; while the red dotted region highlights the abnormality criterion of the deformation.

4.2. Tracking of mesh vertices

Diffeomorphic registrations are performed using the software package *deformetrica* www.deformetrica.org. The parameters of the registration algorithm are set as follows : the standard deviation of the Gaussian kernel defined in (1) is set to $\sigma = 10^{-4}$ in order to obtain a deformation field with a very thin level of precision. The kernel-width parameter for controlling the granularity of the deformation is set to 8. 15 intermediate states describing the temporal evolution of the tracked points are estimated in order to obtain a smooth continuous-time trajectory of the organ between successive time frames. The loss function defined in (5) is minimized using the gradient descent optimization method. All experiments are performed on an Intel[®] Xeon[®] Processor Silver 4214 CPU @ 2.20GHz, with a physical memory of 93GB. For the first subject for example, Algorithm 1 takes 6 sec to align a set of 342 tracked point set \mathcal{M}_t , with the target set \mathcal{C}_t , composed of 5686 points for which only a set of 210 control points have been used for optimizing the shape matching.

To validate the tracking process, we propose to compute the following error :

$$E = \frac{1}{N} \sum_{p=1}^N dist(x_p, \mathcal{C}_L) \quad (14)$$

where N is the total number of tracked points; $x_p \in \mathcal{M}_L$; and $dist(x_p, \mathcal{C}_L)$ is the Euclidean ℓ^2 distance between x_p and the closest point x_l in the last reconstructed contour \mathcal{C}_L . A propagated mean error of 0.63 ± 0.06 is obtained across all subjects. The resulting error is always inferior to $1mm$ which reflects the tracking accuracy level for a given isotropic voxel size of $1 \times 1 \times 1mm$. Fig. 5 shows the quality of our 3D+t quadrilateral mesh reconstruction based on smoothly tracking vertices using the LDDMM while keeping the mesh faces unchanged.

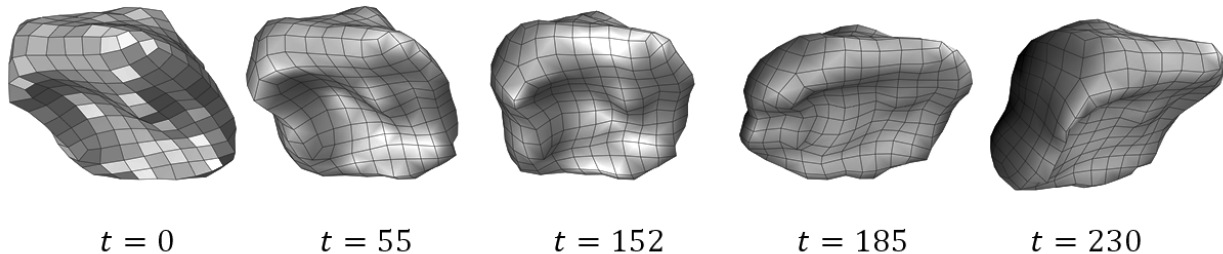


FIGURE 5 – 4D reconstructed quad mesh during forced respiratory motion.

4.3. Geometric descriptors

In this study, we have used different spatio-temporal shape descriptors that can be classified into two categories :

- Biomechanical descriptors : the deformations are quantified using mesh temporal elongations and distortions. This aimed to extend the methodologies used in [34] from 2D+t to 3D+t.
- Geometric descriptors (family of geodesic-based features) : which are the mean curvature and the new proposed feature. This approach allows for taking into account the non Euclidean geometry of three dimensional shape space.

Figure 7 illustrates the capability of each feature to provide a specific information about organ temporal deformation. Both mean curvature and our feature provide information about surfacic tangential deformations. The dihedral angle based distortion may capture mesh sharp deformations, while the mesh elongation aims to capture shape dilations and contractions during motion. For all healthy subjects, the organ is highly deformed by maximum of inspiration and the deformations occur essentially on the top lateral regions. In terms of topology, the organ shape at the maximum of expiration is very close to the shape at resting state. To evaluate the performances of the proposed feature, we have first applied our algorithm to a set of symmetric and non-symmetric geometries. The results are illustrated in Figure 6.

A comparison between different features is performed where the goal is to assess their robustness and to evaluate their performances in terms of :

- sensitivity to tracking error propagation, related to possible registration biases (*e.g.* small errors which may be caused by the smoothing of the velocity vector field within the LDDMM framework.)

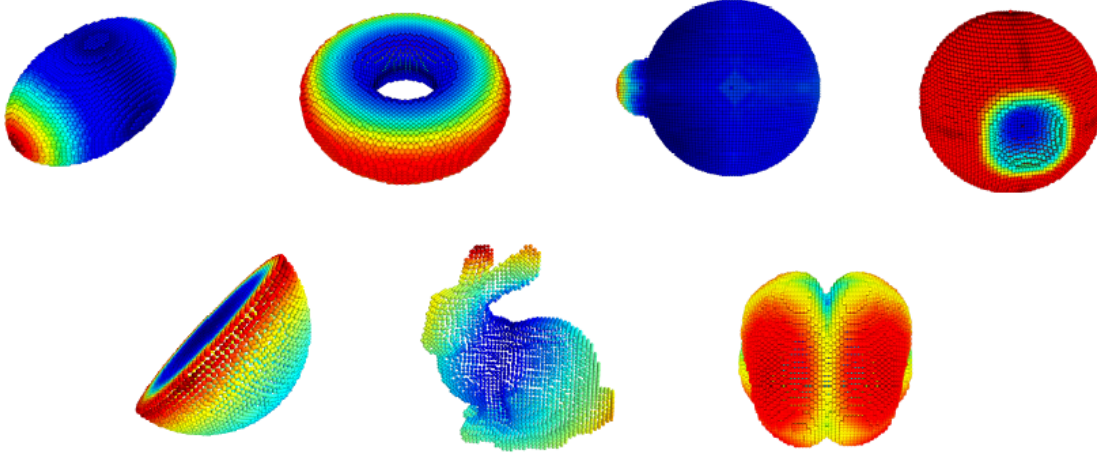


FIGURE 6 – Obtained feature maps for synthetic and realistic 3D shapes.

- Numerical stability throughout a perfectly cyclic nonlinear deformations in the case when the shape trajectory is given *a priori* (*i.e.* using the simulated sequence).

For the simulated sequence, we focus on the similarity between the feature map at the last revisited resting state (towards the end of sequence, $t = 420$), and the reference feature map (at $t=0$). Figure 9 shows that the proposed feature is the more stable since the associated correlation curve reaches its maximum value at each revisited resting state. In fact, the proposed feature exhibit a perfect curve showing a repeated maximum of correlation very close to 1. When the bladder falls down by maximum of inspiration, the application of the proposed feature shows that the organ topology is most deformed laterally.

We have also defined the deformation depth by $Depth = 1 - mincorr$, where $mincorr$ is the minimal correlation achieved at maximum of inspiration (see Figure 9). The obtained subject-specific deformation depths were : 0.12 for mesh elongations, 0.115 for mesh distortions, 0.17 for curvature and 0.36 for the proposed feature. Assuming that we have simulated a large deformation in a specific direction, we remark that the proposed feature is more capable of describing how the maximal deformation through motion is large.

4.4. Subject-specific organ dynamics

Results presented in Fig 8 illustrate the motion pattern dynamics for all subjects using the proposed descriptor. For each motion cycle, a decrease of the correlation value indicates an organ deformation with respect to the reference (initial shape), this can be interpreted by the fact that forced inspiration involves an action of the diaphragm and abdominal muscles that induces deformations of the internal organs. Otherwise, when the correlation values increase, the patient releases the pressure and consequently the bladder relaxes and returns to its initial shape. Respiratory motions were expected to be standard during scanning. However, depth and rhythm may vary across time. The patient’s breathing patterns then becomes irregular with time which can be noticed from the correlation trajectories illustrated in Figure 8.

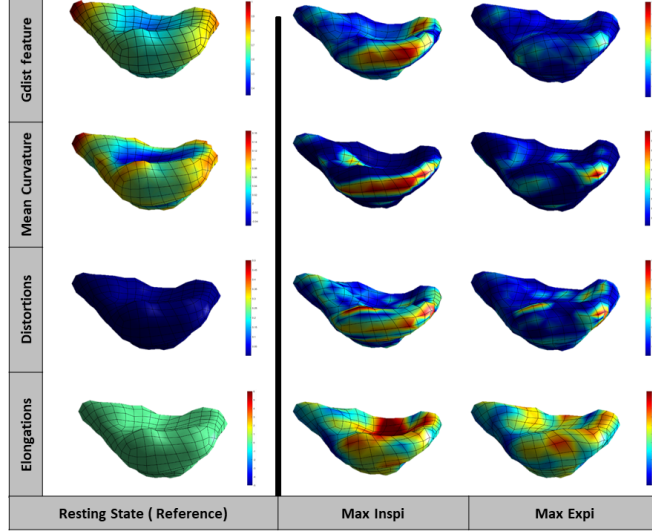


FIGURE 7 – Reference feature maps (left column) and motion patterns or feature differences with respect to the reference at extreme positions (right columns) for one subject.

4.5. Inter-subject variability in motion patterns

In addition to the organ shape inter-variability, depth and rhythm of respiration may vary across subjects. Depending on individual lung functions and capacities, healthy individuals exhibit different motion patterns and thus different bladder volume changes. An inter-subject comparison would be possible by establishing point-to-point anatomical correspondences between these geometric features across subjects.

4.5.1. Maximal-deformation based comparison

Fig. 10 visualises the normalized distance matrices based on the absolute differences of deformation depths between each pair of subjects. The maximal deformation is identified here by the minimum correlation value between the temporal feature vectors w.r.t the reference one, achieved throughout the dynamic sequence, which reflects the maximum of inspiration time where the bladder is deformed the most. When adding the artificial sequence to the data set, it becomes distinguished by having a minimal correlation which is far from those of the realistic sequences. This difference is clearly seen with the proposed feature and with mean curvature, but less clear for the characterization of organ dynamics based on mesh distortions and elongations.

4.5.2. Inter-subject comparison based on the Laplace–Beltrami Operator (LBO) eigenfunctions

Since the mesh resolution differs from one subject to another depending on individual organ shape topologies, the resulting feature vectors with different dimensions (across subjects) are all projected to the same vector space using the LBO eigenfunctions-based spherical mapping method to allow statistical comparisons. We therefore adopted the spherical parameterization method for projecting mesh vertices to the sphere, introduced in [22] by

considering only the three first non-trivial eigenfunctions of the LBO of the closed surfaces, and re-adapted in [23] by taking into account the six first eigenfunctions and then selecting three sorted eigenfunctions with only two nodal domains.

For the proposed geodesic-based feature, the spherical mapping is straightforward since we have the geodesic flow that maps the mesh vertices to the corresponding vertices on a sphere surface (*i.e.* the normal velocity vector field, \vec{T}), and only the interpolation to the unit sphere was required to compute inter-correlations between individuals' motion patterns.

The next step consisted of measuring similarities between individual's motion patterns (*i.e.* between the individual time-average feature vectors) using a temporal inter-subject comparison (vertex-to-vertex) based on a spherical interpolation of vertices and their corresponding texture values to the unit sphere using the Kd-tree interpolation approach included in the Spherical Demons framework [37].

Fig. 11 illustrates the projection of each temporal feature vector on the unit sphere for the simulated sequence. The first column represents the reference feature maps; while the second and third columns represent the feature changes at maximal range of motion w.r.t the reference state.

Figure 12 illustrates the proposed pipeline for measuring the similarity between two shape patterns with different resolution based on the normalized proposed feature.

5. Discussion and conclusion

This study represents an extension of the works of [34] from 2D+t to 3D+t for non-invasively characterizing pelvic floor organ dynamics. In 2D+t, the out of plane problem related to the acquisition protocols and conditions may result a biased characterization of subject-specific motion patterns which makes it difficult to detect regional organ motion abnormalities. Moreover, this natural extension was required because of the variability of abdominal organ shapes across time and subjects. High-resolution temporal reconstruction of bladder volumes was a key factor in the realisation of this work for which the clinically relevant improvement consisted of performing all temporal statistics and measures in the high-resolution domain (*i.e.* a full volume coverage was achieved).

The present study was divided into two main parts :

First, we employed Riemannian geometry for generating shape trajectories belonging to non-linear manifolds through the tracking of geodesically equidistant surface points using the LDDMM framework. Soft tissue organ deformations during motion can be quantified using methods for parametric dynamical systems. The idea behind was to parameterize large deformations with only representative samples of surface points encoding the major shape variability with reasonable computational costs within large datasets. The use of the LDDMM aimed to provide an hypothesis compatible with the physics of deformations (Hamiltonian statistical mechanics). This helped for establishing a compact shape representation relying on 4D smooth quadrilateral meshes for the organ surface with fixed connectivity information. Such realistic reconstructed data will be useful for biomechanical modelling of the organ dynamics and its validation.

The second part consisted of characterizing the bladder shape dynamics during loading exercises through the use of 3D geometric descriptors. Elongations and distortions are a well known biomechanical parameters which have been used in [34] to perform a classification of subjects into two populations : healthy and pathological. However, shape space is a curved surface, and statistical tools derived from Euclidean geometry are not the most appropriate to deal with such clinical issues. For instance, the extension of intrinsic shape signature from 2D to 3D should be avoided since it is not bijective and it depends on mesh resolution (*i.e.* the number of tracked points or vertices). In this work, the shape descriptors used in [34] were first extended to three dimensional space (elongations and distortions) and we have also employed two shape descriptors involving the notion of geodesic distances for a more fine characterization of organ dynamics : the mean curvature and our proposed feature were used to identify salient and non-salient motion patterns.

The mean curvature motion is the most fundamental curve evolution. To study the temporal curvature changes, we have used the method proposed in [38], based on a finite-differences approach for estimating curvatures on irregular triangle meshes. This required the conversion of temporal quad meshes to triangular ones and the major limitation was the dependency of the algorithm on mesh resolution and vertex neighborhood size (this algorithm is well adapted to high-resolution meshes). To cope with this dependency, we proposed the use of a non-parametric Eulerian PDE approach to explore the space of bounded continuous maps from shape surface into a surrounding sphere surface. The derived feature function satisfies the invariance conditions of Kendall’s shape space [20] since it is capable of filtering out translation, scale and rotation.

To analyze descriptors’ performances, we have deformed the bladder volume in the static MRI scan for one subject to simulate a biologically plausible model of abnormal shape trajectory using the LEPF (this aimed to control the deformation kinematics). The results of our experiments on several descriptors show the efficiency and the numerical stability of the proposed shape descriptor for the characterization of surface dynamics for which the efficiency and numerical stability were particularly assessed from its application on a perfectly cyclic nonlinear shape trajectory with a large deformation depth and long-term time variations (see Fig 9).

An inter-individual comparison is also performed by introducing the simulated sequence to the realistic dataset. To make this comparison statistically relevant, shape motion patterns from different descriptors and for different subjects were compared in a common space, the unit sphere, through the use of the LBO eigenfunctions for spherical mapping. Results in Figures 10 and 13 illustrated the fact that motion patterns differs from one subject to another in healthy population and highlighted the capacity of each descriptor to distinguish the abnormal motion type from statistical measures. The results show also that the geodesic-based features (including curvature) are the best classifiers against traditional classifiers based on Euclidean geometry.

All the source codes developed and used in this work are available at <https://github.com/k16makki/dynPelvis/tree/master/Dynpelvis3D>.

Future works will include clinico-pathological data from age-matched women with uterine

and bladder Prolapse. The proposed methods will be employed to identify morphological differences between normal and pathological groups. These techniques could also be applied to study and characterize the dynamics of other functional human tissues and organs such as the heart. A statistical biomechanical modelling of organ dynamics becomes possible by using the obtained dynamical quadrilateral meshes for determining different biomechanical parameters such as strains and stresses in organ functions.

Acknowledgments

This research was supported in part by the AMIDEX - Institut Carnot STAR under the Pelvis3D grant.

References

- [1] Y. M. Law, J. R. Fielding, MRI of pelvic floor dysfunction, *American Journal of Roentgenology* 191 (2008) S45–S53.
- [2] J. Brüning, T. Hildebrandt, W. Heppt, N. Schmidt, H. Lamecker, A. Szengel, N. Amiridze, H. Ramm, M. Bindernagel, S. Zachow, et al., Characterization of the airflow within an average geometry of the healthy human nasal cavity, *Scientific Reports* 10 (2020) 1–12.
- [3] X. Pennec, Advances in geometric statistics for manifold dimension reduction, in : *Handbook of Variational Methods for Nonlinear Geometric Data*, Springer, 2020, pp. 339–359.
- [4] Q. Zheng, H. Delingette, K. Fung, S. E. Petersen, N. Ayache, Unsupervised shape and motion analysis of 3822 cardiac 4D MRIs of UK biobank, *arXiv preprint arXiv :1902.05811* (2019).
- [5] B. Abbas, J. Fishbaugh, C. Petchprapa, R. Lattanzi, G. Gerig, Analysis of the kinematic motion of the wrist from 4D magnetic resonance imaging, in : *Medical Imaging 2019 : Image Processing*, volume 10949, International Society for Optics and Photonics, p. 109491E.
- [6] S. Hong, J. Fishbaugh, G. Gerig, 4D continuous medial representation trajectory estimation for longitudinal shape analysis, in : *International Workshop on Shape in Medical Imaging*, Springer, pp. 125–136.
- [7] K. Makki, B. Borotikar, M. Garetier, S. Brochard, D. B. Salem, F. Rousseau, In vivo ankle joint kinematics from dynamic magnetic resonance imaging using a registration-based framework, *Journal of biomechanics* 86 (2019) 193–203.
- [8] T. Heimann, H.-P. Meinzer, Statistical shape models for 3D medical image segmentation : a review, *Medical image analysis* 13 (2009) 543–563.

- [9] X. Pennec, Statistical analysis of organs' shapes and deformations : the Riemannian and the affine settings in computational anatomy (2020).
- [10] J. Fishbaugh, S. Durrleman, M. Prastawa, G. Gerig, Geodesic shape regression with multiple geometries and sparse parameters, *Medical image analysis* 39 (2017) 1–17.
- [11] M. Zhang, P. Golland, Statistical shape analysis : From landmarks to diffeomorphisms, 2016.
- [12] J. Fishbaugh, M. Prastawa, G. Gerig, S. Durrleman, Geodesic shape regression in the framework of currents, in : *International Conference on Information Processing in Medical Imaging*, Springer, pp. 718–729.
- [13] C. Abi Nader, N. Ayache, P. Robert, M. Lorenzi, A. D. N. Initiative, et al., Monotonic gaussian process for spatio-temporal disease progression modeling in brain imaging data, *NeuroImage* 205 (2020) 116266.
- [14] R. Zolfaghari, N. Epain, C. T. Jin, A. Tew, J. Glaunes, A multiscale LDDMM template algorithm for studying ear shape variations, in : *2014 8th International Conference on Signal Processing and Communication Systems (ICSPCS)*, IEEE, pp. 1–6.
- [15] A. Bône, O. Colliot, S. Durrleman, Learning distributions of shape trajectories from longitudinal datasets : a hierarchical model on a manifold of diffeomorphisms, in : *Proceedings of the IEEE Conference on Computer Vision and Pattern Recognition*, pp. 9271–9280.
- [16] G. Peyré, L. D. Cohen, Geodesic methods for shape and surface processing, in : *Advances in Computational Vision and Medical Image Processing*, Springer, 2009, pp. 29–56.
- [17] D. B. Malament, A remark about the “geodesic principle” in general relativity, in : *Analysis and Interpretation in the Exact Sciences*, Springer, 2012, pp. 245–252.
- [18] Z. Sun, B. P. Lelieveldt, M. Staring, Fast linear geodesic shape regression using coupled logdemons registration, in : *2015 IEEE 12th International Symposium on Biomedical Imaging (ISBI)*, IEEE, pp. 1276–1279.
- [19] H. Kim, M. Styner, J. Piven, G. Gerig, A framework to construct a longitudinal DW-MRI infant atlas based on mixed effects modeling of dODF coefficients, *arXiv preprint arXiv :2003.05091* (2020).
- [20] D. G. Kendall, Shape manifolds, procrustean metrics, and complex projective spaces, *Bulletin of the London mathematical society* 16 (1984) 81–121.
- [21] E. Nava-Yazdani, H.-C. Hege, C. von Tycowicz, A geodesic mixed effects model in Kendall's shape space, in : *Multimodal Brain Image Analysis and Mathematical Foundations of Computational Anatomy*, Springer, 2019, pp. 209–218.

- [22] J. Lefèvre, G. Auzias, Spherical parameterization for genus zero surfaces using Laplace-Beltrami eigenfunctions, in : International Conference on Geometric Science of Information, Springer, pp. 121–129.
- [23] A. Bohi, X. Wang, M. Harrach, M. Dinomais, F. Rousseau, J. Lefèvre, Global perturbation of initial geometry in a biomechanical model of cortical morphogenesis, in : 2019 41st Annual International Conference of the IEEE Engineering in Medicine and Biology Society (EMBC), IEEE, pp. 442–445.
- [24] F. Billet, M. Sermesant, H. Delingette, N. Ayache, Cardiac motion recovery by coupling an electromechanical model and cine-MRI data : First steps, in : Proc. of the Workshop on Computational Biomechanics for Medicine III.(Workshop MICCAI-2008), volume 55, Citeseer, p. 176.
- [25] Z.-W. Chen, P. Joli, Z.-Q. Feng, M. Rahim, N. Pirró, M.-E. Bellemare, Female patient-specific finite element modeling of pelvic organ prolapse (POP), *Journal of biomechanics* 48 (2015) 238–245.
- [26] H. Courtecuisse, Z. Jiang, O. Mayeur, J. Witz, P. Lecomte-Grosbras, M. Cosson, M. Brieu, S. Cotin, Three-dimensional physics-based registration of pelvic system using 2D dynamic magnetic resonance imaging slices, *Strain* 56 (2020) e12339.
- [27] K. Makki, B. Borotikar, M. Garetier, S. Brochard, D. B. Salem, F. Rousseau, High-resolution temporal reconstruction of ankle joint from dynamic MRI, in : 2018 IEEE 15th International Symposium on Biomedical Imaging (ISBI 2018), IEEE, pp. 1297–1300.
- [28] V. Arsigny, O. Commowick, N. Ayache, X. Pennec, A fast and log-euclidean polyaffine framework for locally linear registration, *Journal of Mathematical Imaging and Vision* 33 (2009) 222–238.
- [29] A. C. Ogier, S. Rapacchi, A. Le Troter, M.-E. Bellemare, 3D dynamic MRI for pelvis observation—a first step, in : 2019 IEEE 16th International Symposium on Biomedical Imaging (ISBI 2019), IEEE, pp. 1801–1804.
- [30] K. Makki, A. Bohi, A. C. Ogier, M.-E. Bellemare, A new geodesic-based feature for characterization of 3D shapes : application to soft tissue organ temporal deformations, 25th International Conference on Pattern Recognition (ICPR2020), Jan 2021, Milan, Italy (2020).
- [31] T. Lewiner, H. Lopes, A. W. Vieira, G. Tavares, Efficient implementation of marching cubes’ cases with topological guarantees, *Journal of graphics tools* 8 (2003) 1–15.
- [32] W. Jakob, M. Tarini, D. Panozzo, O. Sorkine-Hornung, Instant field-aligned meshes., *ACM Trans. Graph.* 34 (2015) 189–1.

- [33] M. F. Beg, M. I. Miller, A. Trouvé, L. Younes, Computing large deformation metric mappings via geodesic flows of diffeomorphisms, *International journal of computer vision* 61 (2005) 139–157.
- [34] M. Rahim, M.-E. Bellemare, R. Bulot, N. Pirró, A diffeomorphic mapping based characterization of temporal sequences : application to the pelvic organ dynamics assessment, *Journal of mathematical imaging and vision* 47 (2013) 151–164.
- [35] L. Váša, J. Rus, Dihedral angle mesh error : a fast perception correlated distortion measure for fixed connectivity triangle meshes, in : *Computer Graphics Forum*, volume 31, Wiley Online Library, pp. 1715–1724.
- [36] A. J. Yezzi, J. L. Prince, An Eulerian PDE approach for computing tissue thickness, *IEEE transactions on medical imaging* 22 (2003) 1332–1339.
- [37] B. T. Yeo, M. R. Sabuncu, T. Vercauteren, N. Ayache, B. Fischl, P. Golland, Spherical demons : fast diffeomorphic landmark-free surface registration, *IEEE transactions on medical imaging* 29 (2009) 650–668.
- [38] S. Rusinkiewicz, Estimating curvatures and their derivatives on triangle meshes, in : *Proceedings. 2nd International Symposium on 3D Data Processing, Visualization and Transmission, 2004. 3DPVT 2004.*, IEEE, pp. 486–493.

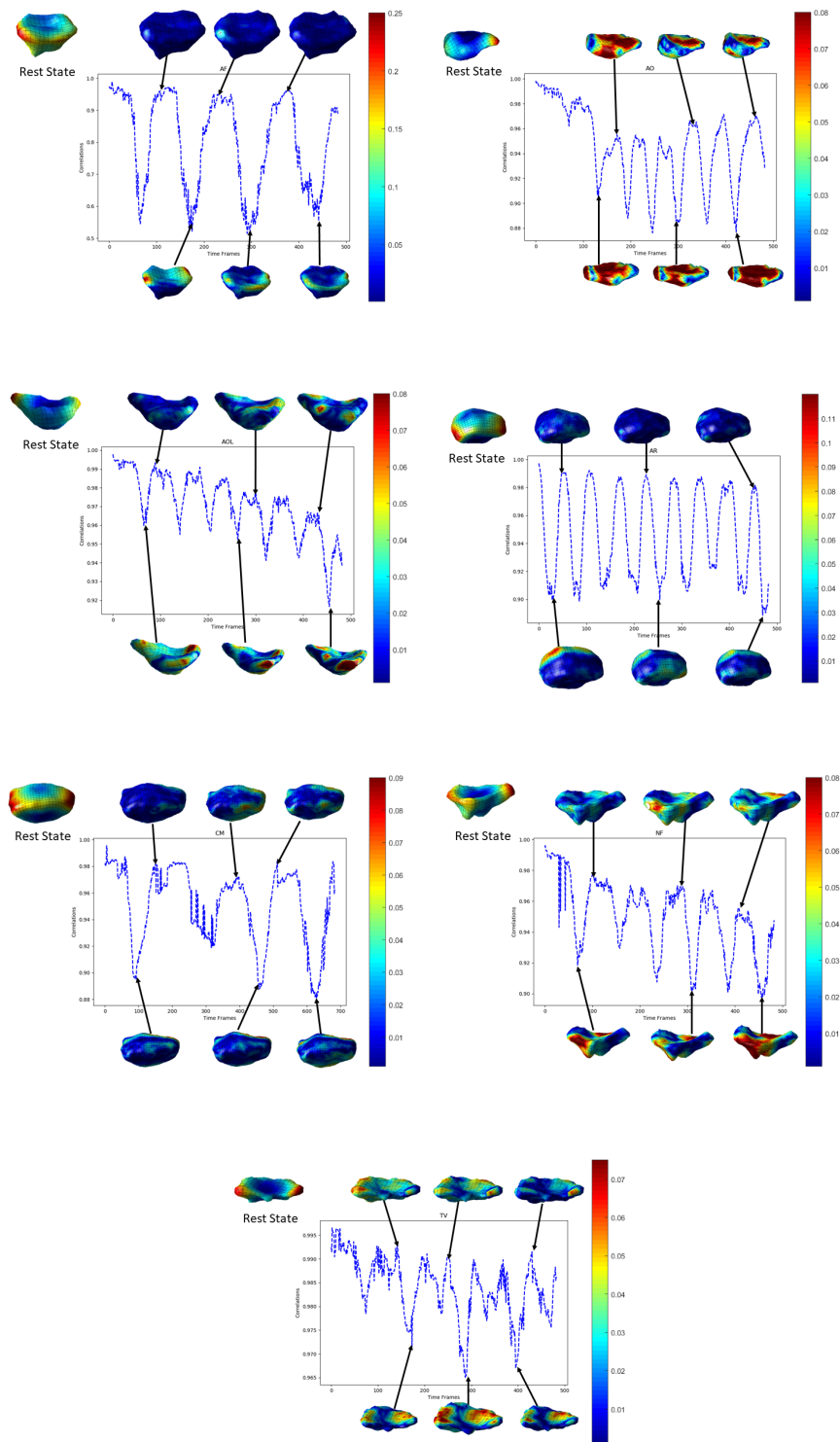


FIGURE 8 – Characterization of the different loading phases of the bladder using the proposed feature + shape motion patterns at max. inspiration and max. expiration.

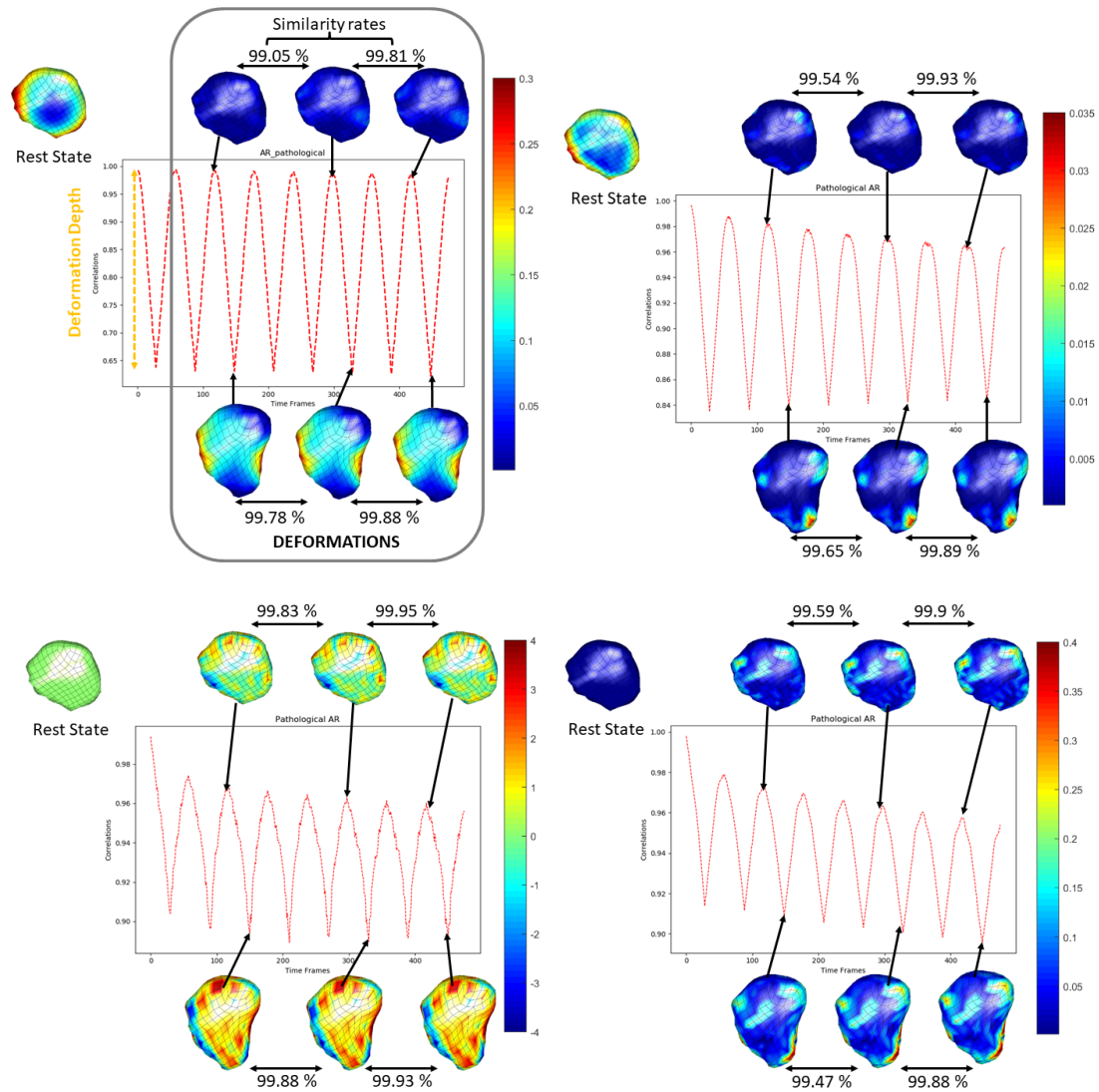


FIGURE 9 – Feature map dynamics w.r.t the resting state. From up to down, from left to right : our feature ; mean curvature ; elongations ; and distortions.

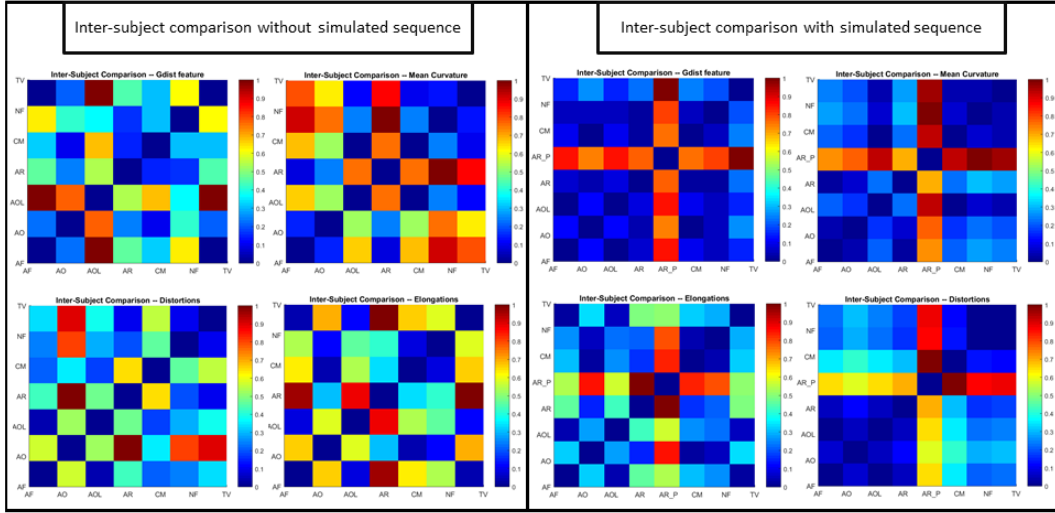


FIGURE 10 – Inter-subject comparison using normalized distance matrices between maximal temporal deformations (i.e. deformation depths). From left to right, from up to down : using the proposed feature, using the mean curvature, using mesh distortions, and using mesh elongations.

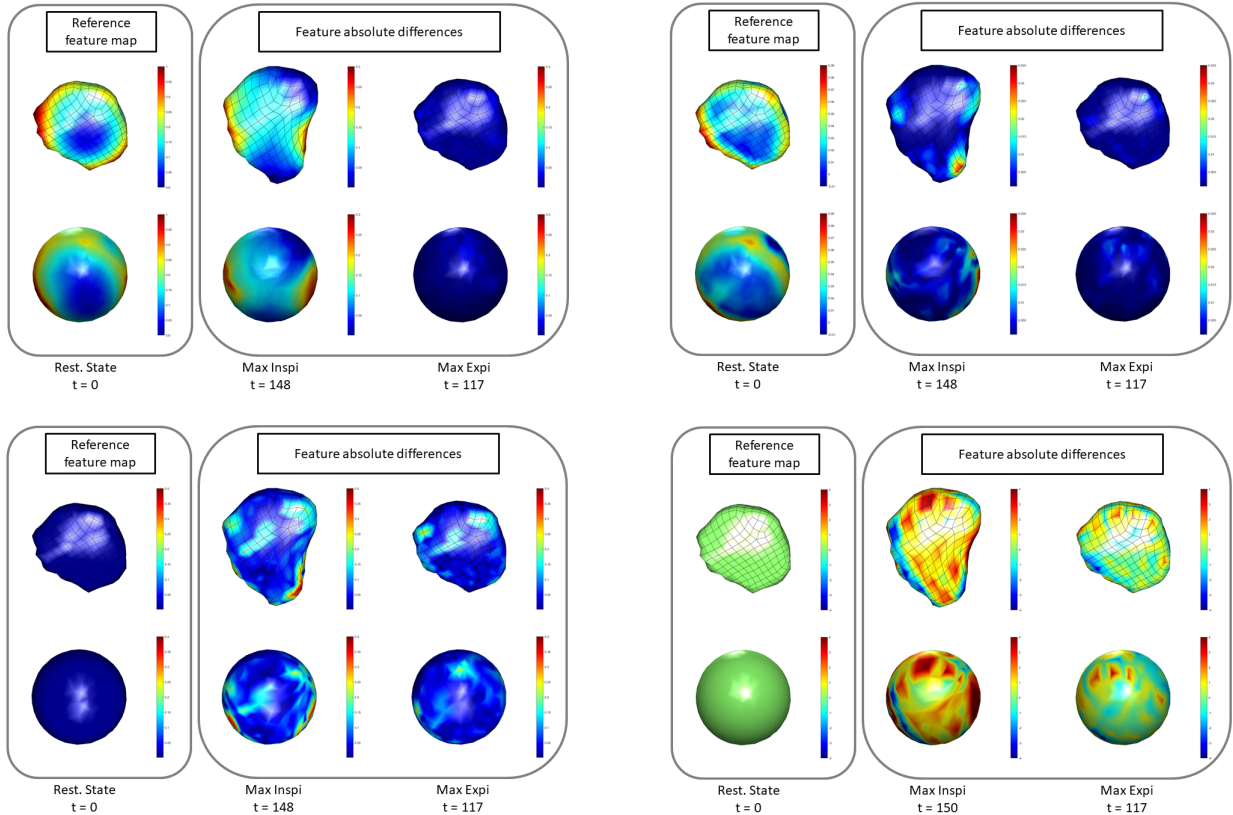


FIGURE 11 – Feature projection on the sphere : 1st column : reference feature map ; 2nd and 3rd columns : feature absolute differences w.r.t the reference (deformation patterns).

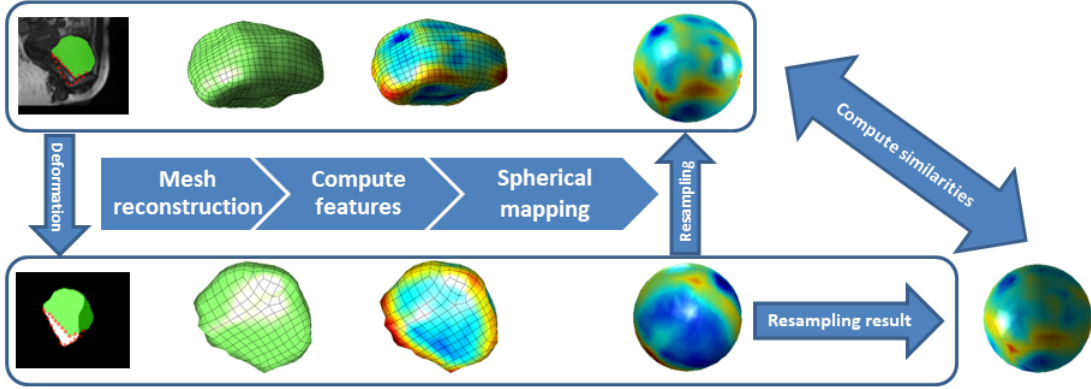


FIGURE 12 – Proposed pipeline for comparing two bladder surfaces. Colormap goes from blue (0) to red (1).

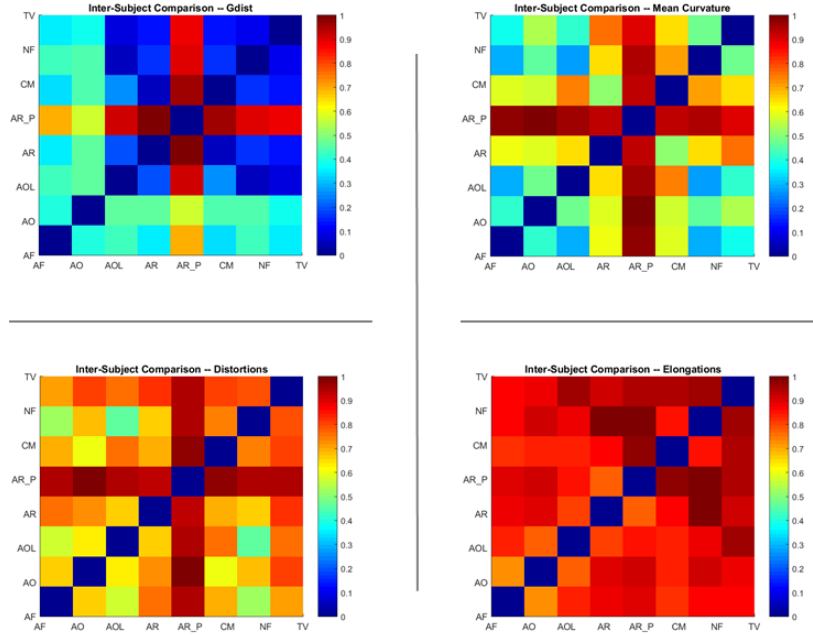


FIGURE 13 – Inter-subject comparison using LBO spherical mapping with a Kdtree interpolation. Comparisons were based on the correlations between subjects’ motion patterns in a common shape space (the unit sphere) : For each feature, the matrix elements were filled using the distance function $dist(\bar{\mathcal{F}}_i, \bar{\mathcal{F}}_j) = 1 - normcorr(\bar{\mathcal{F}}_i, \bar{\mathcal{F}}_j)$, where $\bar{\mathcal{F}}_i$ is the resampled average map for distances between temporal feature vectors and the reference one, for subject i ; and $normcorr$ is the normalized correlation function.